A Simple Phenyl Group Introduced at the Tail of Alkyl Side Chains of Small Molecular Acceptors: New Strategy to Balance the Crystallinity of Acceptors and Miscibility of Bulk Heterojunction Enabling Highly Efficient Organic Solar Cells

Yonghai Li,* Nan Zheng, Lu Yu, Shuguang Wen, Chenglin Gao, Mingliang Sun, and Renqiang Yang*

Research on fused-ring small-molecular-acceptors (SMAs) has deeply advanced the development of organic solar cells (OSCs). Compared to fruitful studies of ladder-type cores and end-caps of SMAs, the exploration of side chains is monotonous. The widely utilized alkyl and aryl side chains usually produce a conflicting association between SMAs' crystallinity and miscibility. Herein, a fresh idea about the modification of side chains is reported to explore the subtle balance between the crystallinity and miscibility. Specifically, a phenyl is introduced to the tail of the alkyl side chain whereby a new acceptor IDIC-C4Ph is reported. Moderately weakened crystallinity is observed, while maintaining preferred absorption profiles and face-on orientations. Concurrently, remarkably improved heterojunction morphologies and stacking orientations are detected. PBDB-T:IDIC-C4Ph devices exhibit greater efficiency of 11.50% than devices from alky and aryl modified acceptors. Notably, the as-cast OSCs of PBDB-TF:IDIC-C4Ph reveal outstanding FF over 76% with the best efficiency up to 13.23%. The annealed devices reveal further increased efficiency exceeding 14% with the state of the art FF of 78.32%. Overall, an effective but easily navigable approach is demonstrated to modulate the crystallinity of SMAs toward synergistically improved morphologies and molecular orientations of bulk heterojunction enabling highly efficient OSCs.

The development of nonfullerene small molecular acceptors (SMAs) with advantages of easy-tailored absorption properties and frontier energy levels has seen impressive progress since 2015.[1] Considerable efforts have been dedicated to the research of new SMAs. Recently, power conversion efficiencies (PCEs) over 14% have been realized in single bulk-heterojunction (BHJ) organic solar cells (OSCs).[2–4] Thus it is believed that the development of efficient SMAs is highly promising for the future practical application of OSCs.

Generally, SMAs were built with a ladder-type electron-rich core, flanked by two electron-deficient end caps and several side chains attached onto the sp^3 carbon of the core (Scheme S1, Supporting Information). The core affords a rigid conjugated molecular plane and facilitates the molecular stacking. In principle, most of the ladder-type structures could qualify the core and diverse SMAs with the arene number varying from 5 to 12 have been continuously developed.[1,5–13] As for end caps, IC (2-methylene-(3-(1,1-dicyanomethylene)indanone)) unit was one of the most widely used structures.[1] For example, with IC as the end cap, indacenodithiophene (IDT) and indacenodithieno[3,2-b]thiophene (IDTT) as the ladder-type cores, the resulting SMAs were known as 2,2′-((2Z, 2′Z)-((4,4,9,9-tetrahexyl-4,9-dihydro-s-indaceno[1,2b:5,6-b′]dithiophene-2,7-diyl)bis(methanylylidene))bis(3-oxo- 2,3-dihydro-1H-indene-2,1-diylidene))dimalononitrile

Dr. Y. Li, L. Yu, Dr. S. Wen, C. Gao, Prof. R. Yang
CAS Key Laboratory of Bio-Based Materials
Qingdao Institute of Bioenergy and Bioprocess Technology
Chinese Academy of Sciences
Qingdao 266101, China
E-mail: liyh@qibebt.ac.cn; yangrq@qibebt.ac.cn

The ORCID identification number(s) for the author(s) of this article can be found under https://doi.org/10.1002/adma.201807832.

Dr. N. Zheng
State Key Laboratory of Luminescent Materials and Devices
South China University of Technology
Guangzhou 510640, China

L. Yu, Prof. M. Sun
Institute of Material Science and Engineering
Ocean University of China
Qingdao 266100, China

ADVANCED
SCIENCE NEWS

www.advancedsciencenews.com

ADVANCED
MATERIALS

www.advmat.de

(IDIC) and 2,2′-[[6,6,12,12-tetrakis(4-hexylphenyl)-6,12-dihydrodithieno[2,3d:2′,3′-d′]-s-indaceno[1,2-b:5,6-b′]dithiophene-2,8diyl]bis[methylidyne(3-oxo-1H-indene-2,1(3H)diylidene)]]bis[propanedinitrile] (ITIC), respectively.[1,5] Hou and co-workers found that the introduction of electron-donating substitutions including methyl and methoxyl groups at the 5,6-positions of the benzene of IC could upshift the highest occupied molecular orbital (HOMO) and lowest unoccupied molecular orbital (LUMO) energy levels of the SMAs.[14,15] Thus, the fabricated OSCs produced improved open-circuit volt- ages (V_{OC}). On the contrary, the electron-withdrawing substitu- tions at IC, for example, the fluorine and chlorine atoms, would downshift the LUMO level and narrow the optical bandgaps of SMAs. Thus reduced V_{OC} but increased short-circuit current densities (J_{SC}) were currently detected from the resulting OSCs. For example, when IT-4Cl was blended with donor PBDB-TF, the OSCs exhibited inferior V_{OC} of 0.790 V, but fairly high J_{SC} of 22.67 mA cm^{-2} and PCE of 13.45%.[4] Yang and co-workers developed a new end-cap structure CPTCN instead of IC, by replacing benzene of IC with thiophene.[16] Again, substitutions with tuned electronic properties were utilized to enable excellent OSCs.[17,18] In some cases, an electron-rich or electron-deficient π-bridge would be inserted between the core and end cap to tune the properties of SMAs.[19–21] To some extent it is predictable about the tailor of V_{OC} and J_{SC} of OSCs related to the energy levels and absorption spectra of SMAs. However, it is still challenging to precisely predict and modulate the molecular stacking of SMAs and BHJ morphologies which is closely related to the fill factor (FF) of OSCs. There are increasing reports of OSCs with decent V_{OC} around 0.85 V and J_{SC} around 20 mA cm^{-2}, but moderate FF around 70%.[11,21–24] This gradually turns to be an obstacle for the development of OSCs with the state-of-the-art PCEs.

For SMAs, it should be noted that the several (four, in most cases) side chains attached onto the sp^3 carbon of the ladder-type core not only increase the solubility and film-forming characteristics of SMAs, but also modulate the intermolecular interactions, optical nature, and BHJ morphology properties. For most of SMAs reported so far, alkyl chains and aryl chains (aryl group attached onto the backbone, with alkyl chain on other positions of aryl group) are the widely utilized side chains (see Scheme S1 in the Supporting Information).[1,5] For instance, the side chains of ITIC are four p-hexylphenyl with phenyl attached at the 4,4,9,9-positions of IDTT core.[1] Li and co-workers reported m-ITIC in which the side chains are m-hexylphenyl groups.[25] Marks and co-workers investigated the influence of alkyl substituent dimensions on the para-position of the phenyl side groups of ITIC.[26] Additionally, ITIC-Th was also reported with the side chain 5-hexylthiophenyl.[27] The bulky aryl side groups are favored in most SMAs (especially for those with large backbones) because the bulky side chains can effectively prevent the acceptor molecules from forming H-aggregates and increase the miscibility with various donors. However, the bulky aryl groups close to the backbone inevitably lead to larger π–π stacking distance and decrease the instinct electron mobility. Inferior FF could be observed in OSCs with aryl-substituted SMAs especially those with smaller arene backbones. Yang and co-workers reported hexyl-substituted SMA IDTPC that exhibited higher

extinction coefficient, redshifted absorption, and stronger face-on orientation than the analog p-hexylphenyl-modified IDTCN. Greater PCE was recorded in IDTPC-based OSCs benefiting from the remarkable enhanced J_{SC} (13.9–17.5 mA cm^{-2}) and FF (54.0–74.6%) values.[28] Similar tendency was observed in ITIC and octyl-substitued C8-ITIC reported by Heeney's group.[29]

Comparing with the bulky aryl side groups, alkyl-modified SMAs can ensure the stronger intermolecular interaction and shorter π–π stacking distance. However, the compact and well-aligned alkyl chains could induce excessive aggregation, which would harm the solubilities of SMAs, decrease the miscibility, and lead to large domain size in BHJ blends. To combine both the merits of alkyl and aryl side chains, Bo and co-workers reported a new SMA IDT-OB carrying aryl p-hexylphenyl and n-octyl alkyl chains at the same sp^3 carbon of the IDT core. Obviously decreased crystallinity of IDT-OB was detected compared to alkyl-substituted IDT-2O.[30] As a result, BHJ based on IDT-OB produced better nanofibrillar networks yielding higher J_{SC} and PCE than IDT-2O based OSCs in which strong aggregation and large domains were observed. However, it should be noted that the crystallinity of IDT-OB probably be overly weakened by the maintained one aryl chain and the resulting stereoisomers, which makes the absorption spectrum of IDT-OB blueshift by about 10 nm than alkyl-substituted analog. Thus, the FF of IDT-OB-based device was slightly decreased relative to IDT-2O device and J_{SC} was negatively influenced duo to the narrowed absorption range. Nevertheless, these results indicate that there is growing consensus about the tailor of SMAs' side chains and the potential to improve PCEs of OSCs.

For SMAs, the ladder-type cores have been heavily studied and diverse building blocks with tuned electron properties are constantly being reported. Meanwhile, the end caps have been efficiently developed. However, as pointed out above, the research of side chains of SMAs is monotonous and heavily dragged behind. Despite there have been tremendous and effective reports about the side chain modification of donor semiconductors,[31–36] these results could be invalid even false in SMAs for their inherent distinction of molecular construction. For most of the donor materials, the main backbones were built by π–σ–π type with the electron-rich, π-spacers and electron-deficient moieties connected by rotatable single bands. The π–σ–π-type backbones usually promise with good flexibility and weaker crystallinity of materials. Thus, the side chain engineering of donor materials mainly focuses on the enhancement of crystallinity and intermolecular interactions.[36–38] While for SMAs, the plane of the molecular backbone is locked by the sp^3 carbon of the core and vinyl attached to the end caps. The rigid plane of the backbone could induce strong self-aggregation of SMAs especially with the aid of compact alkyl side chains. Hence, it is still challenging to precisely modulate the side chains of SMAs to achieve a compromise between the crystallinity of acceptor and its miscibility with donor materials.

Herein, we focus our endeavor to solve this dilemma. We employed the classical acceptors IDIC and IDIC-PhC6, substituted with alkyl and aryl side chains, respectively, as the control acceptors. Inventively, we attached an aryl group (phenyl)

ADVANCED
SCIENCE NEWS
www.advancedsciencenews.com

ADVANCED
MATERIALS
www.advmat.de
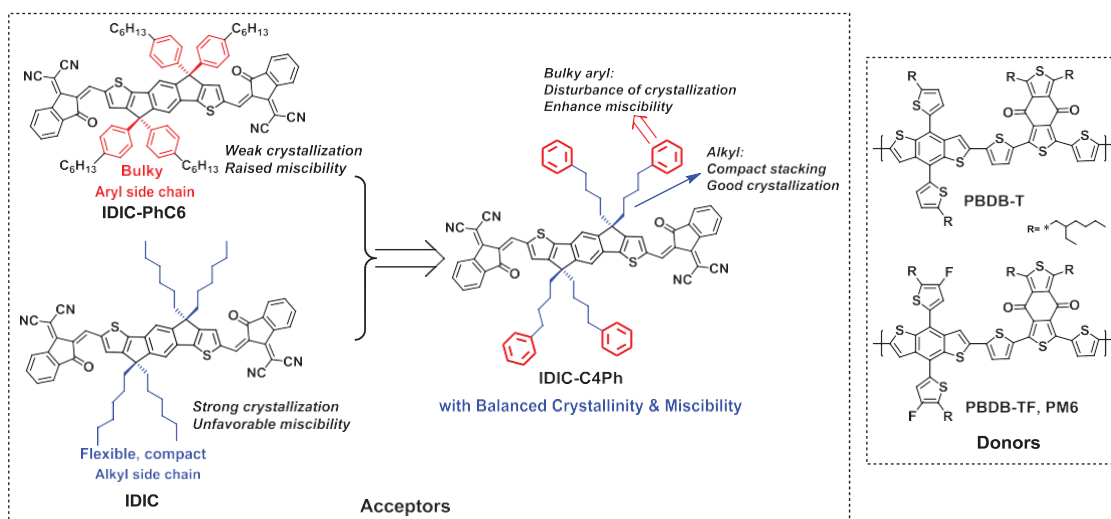
Scheme 1. Chemical structures of SMAs (IDIC-PhC6, IDIC, and IDIC-C4Ph) and donors (PBDB-T and PBDB-TF).

at the tail of the alkyl chain (核C_4H_9) which is easy to imple- ment, and thereby reported a new SMA IDIC-C4Ph as dis- played in **Scheme 1**. The side chain type of IDIC-C4Ph, from the other perspective, can also be considered as the inversion of the side chain of IDIC-PhC6, with the bulky phenyl pushed away from the molecular backbone. Conceptually, the linear *n*-butyl attached onto the IDT was expected to ensure the close molecular stacking and decent crystallinity. Simultaneously, the bulky phenyl at the terminal of *n*-butyl was introduced to alleviate the crystallinity, preventing the excessive aggregation of SMA and increasing the miscibility with donor materials. As we designed, IDIC-C4Ph exhibits moderately weakened crystallinity than IDIC, but stronger than that of IDIC-PhC6. Moreover, IDIC-C4Ph keeps the nearly identical optical prop- erties with IDIC. Excitingly, the decreased crystallinity of IDIC-C4Ph does not disturb the molecular orientations in BHJ, but generates preferred strong face-on orientation and well- distributed nanofibrous morphology in BHJ. Low efficiency of 6.14% was observed in PBDB-T:IDIC-PhC6-based devices with poor FF below 60%. While PBDB-T:IDIC-based devices exhib- ited the optimal PCE of 10.41% with enhanced FF of 73.60%. Intriguingly, PBDB-T:IDIC-C4Ph devices revealed the best PCE up to 11.50%, with improved J_{SC} of 18.08 mA cm^{-2} and high FF of 77.42%. To further verify this strategy and improve the

PCEs, donor PBDB-TF with a deeper HOMO energy level was employed. As a result, improved V_{OC} while still keeping high FF was detected from PBDB-TF-based OSCs. It is worth high- lighting that fairly high PCE up to 13.23% was recorded from PBDB-TF:IDIC-C4Ph built as-cast OSCs, with a V_{OC} of 0.952 V, a J_{SC} of 18.10 mA cm^{-2}, and an outstanding FF of 76.83%. To the best of our knowledge, this is the highest FF and one of the topmost efficiencies among as-cast OSCs, surpassing PBDB-TF:IDIC-based as-cast solar cells (PCE of 12.02%, V_{OC} of 0.947 V, J_{SC} of 18.17 mA cm^{-2}, and FF of 69.88%). After thermal annealing, the state-of-the-art PCE of 14.04% was obtained with a V_{OC} of 0.941 V, a J_{SC} of 19.06 mA cm^{-2}, and an FF of 78.32%. Overall, this study provided a new insight on the rational modulation of side chains of SMAs, and reported an effective but simple approach to reach a subtle balance between SMA' crystallinity and the miscibility enabling high efficiencies of OSCs.

For the three SMAs, IDIC-PhC6 and IDIC were synthesized according to previous reports.[5,39] The synthetic approach of IDIC-C4Ph is displayed in Scheme S2 (Supporting Informa- tion). The UV–vis absorption spectra of three SMAs in chloro- form and as films are shown in **Figure 1**a,b. IDIC-C4Ph keeps overlapping absorption profiles with IDIC in solutions. More importantly, IDIC-C4Ph and IDIC reveal almost identical film
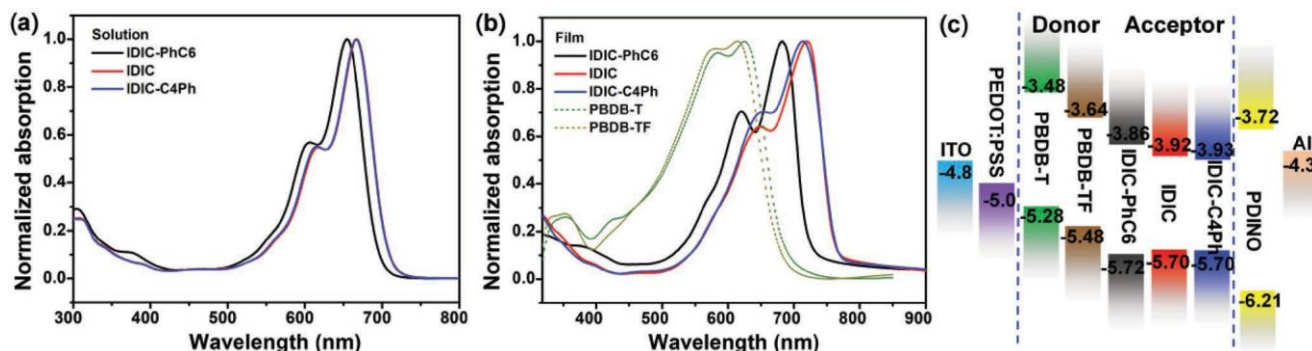
Figure 1. a) Absorption spectra of IDIC-PhC6, IDIC, and IDIC-C4Ph in chloroform; b) film absorption spectra of SMAs and donors PBDB-T and PBDB-TF; c) the energy band diagram.

Table 1. Optical properties and frontier energy levels of three acceptors.

Acceptor	λ_{max} [nm]		$\varepsilon_{solution}$	ε_{film}	E_g^{opt}	HOMO/LUMO	E_g^{cv}
	Solution	Film	$(10^5 \text{ m}^{-1} \text{cm}^{-1})$	(10^5 cm^{-1})	[eV][a)]	[eV]	[eV]
IDIC-PhC6	654	682	1.48	1.08	1.71	−5.72/−3.86	1.86
IDIC	666	716	2.20	1.31	1.63	−5.70/−3.92	1.78
IDIC-C4Ph	666	714	1.81	1.33	1.62	−5.70/−3.93	1.77

[a)]Calculated from the onset wavelength of thin film absorption spectra.

absorption spectra, which is a great advance relative to the asymmetrical side chain modification as reported before.[30] Noticeably, despite a lower extinction coefficient (ε) in solution, the ε values of IDIC-C4Ph and IDIC as films are proximate (1.33 × 10^5 and 1.31 × 10^5 cm^{-1}, respectively) (Figure S1, Supporting Information). The almost unchanged absorption spectra and extinction coefficient of IDIC-C4Ph were critical for OSCs reaching its maximum J_{SC}. As for IDIC-PhC6, the blueshifted absorption spectra in solution and as film suggested remarkably weakened intermolecular interactions ascribing to the significant steric hindrance of aryl side chains. Similar results have been reported in previous work involved in aryl- and alkyl-substituted SMA analog.[28,29,40] The absorption spectra of the donor materials (PBDB-T and PBDB-TF) utilized in this work were also measured and incorporated into Figure 1b. The slightly blueshifted spectrum of PBDB-TF was helpful to the OSCs to cover expanded solar spectrum and generate an improved J_{SC}. The molecular energy levels of SMAs were measured by cyclic voltammetry (CV) and are displayed in Figure S2 (Supporting Information) and **Table 1**. The results show that three SMAs keep the similar HOMO and LUMO energy levels indicating a minor effect of side chains.

Thermogravimetric analysis (TGA) traces (Figure S3, Supporting Information) indicate that IDIC-PhC6, IDIC, and IDIC-C4Ph are of good thermal stability with the decomposition temperature (5% weight loss) around 330 °C. Differential scanning calorimetry (DSC) was further performed to roughly evaluate the crystallization process of three acceptors and the DSC curves are displayed in Figure S4 (Supporting Information). No any distinct endothermic or exothermic transition was detected from the DSC curve of IDIC-PhC6, indicating a weak crystallization tendency. As for IDIC, it displays a strong tendency to crystalize with sharp crystallization transition in the first heating cycle related to the cold crystallization transition according to previous report.[8,26] A similar crystallization transition with much lower enthalpy change was observed for IDIC-C4Ph. This could indicate a decreased crystallinity for IDIC-C4Ph compared to IDIC, originating from the disturbance of the phenyl group at the tail of the alkyl side chains.

In order to obtain deep insights into the crystallization behaviors and molecular stacking orientations of three SMAs, grazing incidence wide angle X-ray scattering (GIWAXS) was implemented on the films of IDIC-PhC6, IDIC, and IDIC-C4Ph and is displayed in **Figure 2**. As shown in Figure 2a, only
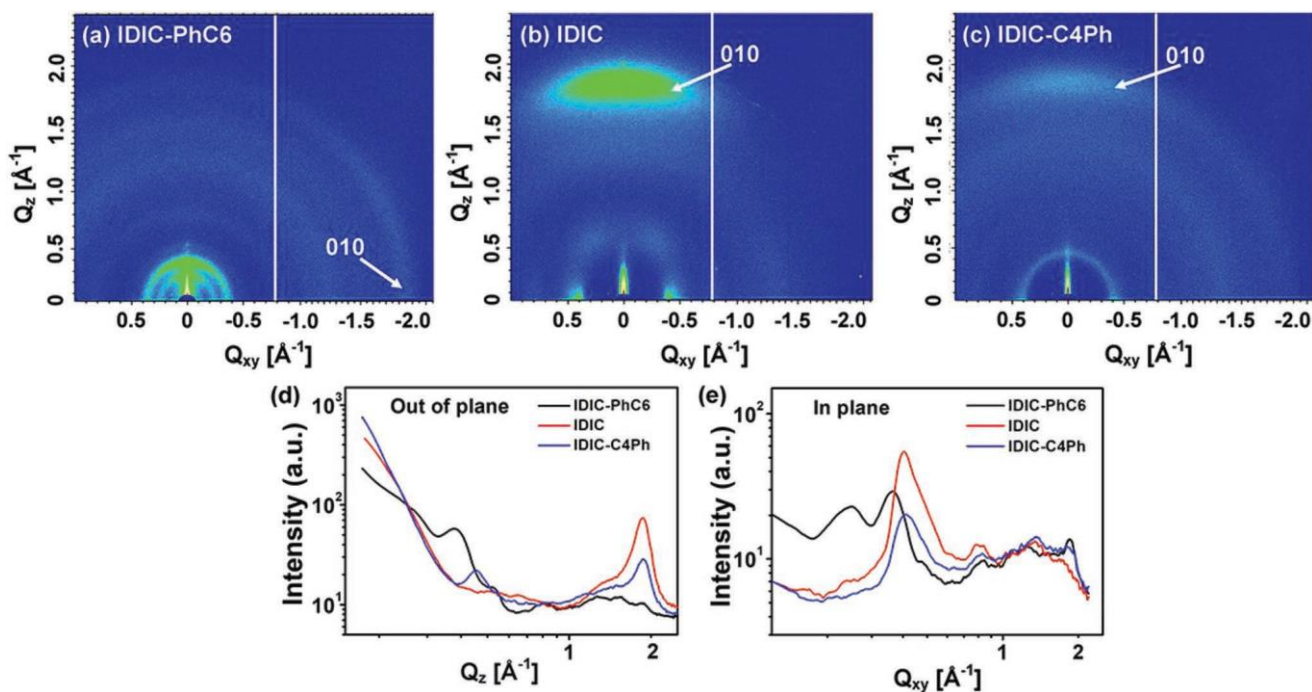
Figure 2. GIWAXS scattering patterns of a) IDIC-PhC6, b) IDIC, and c) IDIC-C4Ph; the line profiles of GIWAXS d) out of plane and e) in plane.

ADVANCED
SCIENCE NEWS
www.advancedsciencenews.com

ADVANCED
MATERIALS
www.advmat.de

Table 2. Device parameters of OSCs under the illumination of AM 1.5G, 100 mW cm^{-2}.

| Blend		V_{OC} [V]	J_{SC} [mA cm^{-2}]	(J_{SC}^{EQE}) [a)]	FF [%]	PCE [%][b)]	μ_h/μ_e 10^{-4} cm^2 V^{-1} s^{-1}
PBDB-T:IDIC-PhC6	TA	0.869 (0.863 ± 0.005)	12.20 (12.03 ± 0.38)	10.85	57.90 (56.80 ± 1.25)	6.14 (5.92 ± 0.20)	2.31/0.02
PBDB-T:IDIC	TA	0.819 (0.812 ± 0.009)	17.27 (17.13 ± 0.31)	16.68	73.60 (72.51 ± 1.34)	10.41 (10.10 ± 0.31)	2.42/2.90
PBDB-T:IDIC-C4Ph	TA	0.822 (0.810 ± 0.011)	18.08 (17.93 ± 0.18)	17.44	77.42 (75.92 ± 1.86)	11.50 (11.33 ± 0.19)	4.70/4.89
PBDB-TF:IDIC-C4Ph	As-cast	0.952 (0.941 ± 0.010)	18.10 (17.78 ± 0.25)	17.37	76.83 (75.20 ± 1.44)	13.23 (13.03 ± 0.28)	2.21/2.66
PBDB-TF:IDIC-C4Ph	TA[c)]	0.941 (0.935 ± 0.007)	19.06 (18.92 ± 0.33)	18.34	78.32 (77.20 ± 0.86)	14.04 (13.72 ± 0.26)	3.48/4.51
PBDB-TF:IDIC-C4Ph	TA[c)]+DIO	0.929 (0.920 ± 0.007)	18.91 (18.72 ± 0.27)	–	77.10 (76.35 ± 0.78)	13.54 (13.31 ± 0.28)	–
PBDB-TF:IDIC	As-cast	0.947 (0.940 ± 0.008)	18.17 (17.90 ± 0.36)	17.53	69.88 (68.69 ± 1.25)	12.02 (11.69 ± 0.34)	1.76/1.85
PBDB-TF:IDIC	TA[c)]	0.935 (0.929 ± 0.007)	17.71 (17.63 ± 0.22)	–	68.16 (67.20 ± 0.98)	11.28 (11.02 ± 0.30)	0.47/3.80
PM6:IDIC[d)]	As-cast	0.97	17.8	17.2	69	11.9 (11.7)	–

[a)]Integrated from the EQE spectrum; [b)]Average values with standard deviations were obtained from at least 15 cells; [c)]Thermal annealing at 130 °C for 30 s. For other TA in the table, TA: thermal annealing at 130 °C for 5 min; [d)]Extracted from the previous report[41]; PM6 and PBDB-TF represent the same material.

discernible π–π stacking diffraction plot along the in plane (IP) direction was observed, signifying part of edge-on orientations of film IDIC-PhC6. Moreover, the laminar packing distance in IP direction was calculated to be 25.2 Å, much bigger than those of IDIC (15.5 Å) and IDIC-C4Ph (15.4 Å), indicating the weak intermolecular interactions. From the GIWAXS pattern of IDIC (Figure 2b), strong and well-defined diffraction spot at 1.82 Å in the out-of-plane (OOP) direction was detected. Based on the Scherrer equation calculation, the π–π crystal coherence length (CCL) in OOP and interchain stacking in the IP direction was calculated to be 26.4 and 64.3 Å, respectively. The prominent face-on and orderly laminar stacking of IDIC were partly enhanced by the compact and well-aligned alkyl side chains. For IDIC-C4Ph, the film exhibits weakened π–π stacking diffraction than that of IDIC in the OOP direction (Figure 2d) with a decreased CCL of 22.6 Å. The laminar CCL in the IP direction was also reduced to 53.2 Å. This again demonstrates that the crystallization property of IDIC-C4Ph was to some extent weakened by the disturbance of the bulky aryl terminals of side chains. It is noteworthy that for IDIC-C4Ph and IDIC films both the π–π stacking in the OOP direction are located around 1.82 Å, corresponding to a π–π stacking distance of 3.45 Å. Furthermore, both IDIC-C4Ph and IDIC adopted the dominating face-on stacking orientations in the films and were ordinarily beneficial for the charge transport in the vertical direction of OSCs. Thus, the GIWAXS results of three acceptors show that the aryl terminal of the alkyl side chain could decrease the crystallinity of the material (IDIC-C4Ph), while keeping close π–π stacking distance.

To evaluate the photovoltaic performance of three SMAs, OSC devices with a conventional structure of ITO/PEDOT:PSS/donor:SMA/PDINO/Al were fabricated. Here, PBDB-T was utilized as the donor, and IDIC-PhC6, IDIC, and IDIC-C4Ph were used as the acceptor. The best weight ratios for all the three OSCs were confirmed to be 1:1 (Table S1, Supporting Information) and the optimal photovoltaic properties are collected in **Table 2** and **Figure 3**. As shown in Table 2 and Table S1 (Supporting Information), inferior PCE of 6.14% with low J_{SC} and FF (57.90%) were measured from the PBDB-T:IDIC-PhC6 device. However, solar cells fabricated from PBDB-T:IDIC

provided an increased PCE of 10.41%, with a V_{OC} of 0.819 V, enhanced J_{SC} of 17.27 mA cm^{-2}, and an FF of 73.60%. The photovoltaic performance from IDIC-PhC6- to IDIC-based devices reveals a similar rising tendency with other previous reports involving with aryl-substituted and alkyl-substituted analog SMAs.[28–30,40] Excitingly, the as-cast PBDB-T:IDIC-C4Ph devices generate the best PCE of 10.95%, greater than IDIC-based optimal devices (Table S1, Supporting Information). Especially, after thermal annealing optimization, the efficiency of PBDB-T:IDIC-C4Ph device was further enhanced, yielding the champion PCE up to 11.50% with a V_{OC} of 0.822 V, a J_{SC} of 18.08 mA cm^{-2}, and an FF of 77.42%. Compared to IDIC, IDIC-C4Ph-based OSC generated an improved J_{SC} and impressive FF over 77%, leading to an increased PCE. The external quantum efficiency (EQE) measurements (Figure 3c) of three optimal devices show that the PBDB-T:IDIC-C4Ph-based device exhibited higher EQE response around 700 nm than the other two devices, mainly related to the absorption of SMAs (Figure 1b). In conclusion, combined with the results of crystallization studies of three acceptors, we can discover that the moderately weakened crystallinity of IDIC-C4Ph exhilaratingly greatly improved the FF as well as PCEs of OSCs, which probably correlated with the optimization of BHJ morphologies.

Though impressive PCEs were recorded from PBDB-T:IDIC-C4Ph-based solar cells, the efficiency was apparently suppressed by the relatively low V_{OC} around 0.82 V. Therefore, PBDB-TF (an analog of PBDB-T) with lower HOMO energy level by 0.20 eV than PBDB-T was utilized to raise the V_{OC} of the OSCs and further verify the design idea of this work. As a result, all the PBDB-TF fabricated OSCs demonstrated improved V_{OC} by over 0.1 V than PBDB-T based devices and the PCEs of devices were greatly boosted. It is worth highlighting that excellent FFs with the average value above 75% were recorded from 25 as-cast solar cells fabricated from PBDB-TF:IDIC-C4Ph. The champion as-cast device exerted a high FF of 76.83%, promoting the best PCE to reach 13.23%, with a V_{OC} of 0.952 V and a J_{SC} of 18.10 mA cm^{-2}. To the best of our knowledge, this represents one of the highest PCE recorded from the as-cast OSCs especially with such an outstanding FF (see Figure 3d and Table S2 in the Supporting Information). As
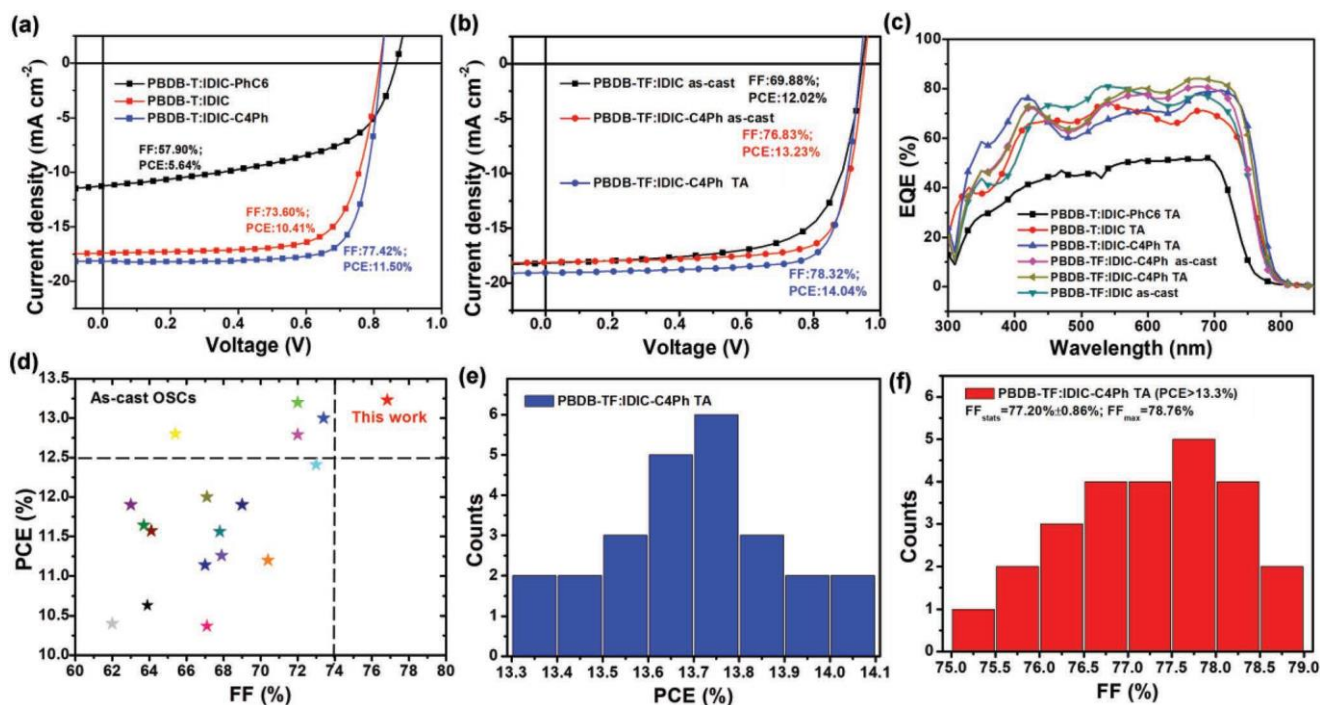
Figure 3. a) The optimal *J–V* curves of PBDB-T:SMA-based devices. b) The *J–V* curves of PBDB-TF:IDIC- and PBDB-TF:IDIC-C4Ph-based devices under different conditions. c) The respective EQE curves. d) Comparison of the photovoltaic properties with representative FF and PCE values reported in the literature and this work (PBDB-TF:IDIC-C4Ph) for as-cast OSCs. The detailed parameters are collected in Table S2 (Supporting Information). e) Statistical PCE and f) FF distribution histograms of the annealed OSCs based on 25 cells of PBDB-TF:IDIC-C4Ph.

a contrast, the control device fabricated from PBDB-TF:IDIC as-cast blend reveals the best PCE of 12.02% with a V_{OC} of 0.947 V, a J_{SC} of 18.17 mA cm^{-2}, and a lower FF of 69.88%, in line with the previous report (see the last row in Table 2, here PM6 and PBDB-TF represent the same material).[41] Like-wise, the thermal annealed PBDB-TF:IDIC-based OSCs afford a decreased PCE of 11.28% which is also consistent with the previous report. Inspiringly, as for PBDB-TF:IDIC-C4Ph-based OSCs, after a quick thermal annealing at 130 °C for 30 s, a further increased J_{SC} and FF, with slightly decreased V_{OC}, were detected (see Table S1 in the Supporting Information). Specifically, the thermal annealed devices exhibit an average PCE of 13.72% based on 25 cells (Figure 3e). Meanwhile, an average FF of 77.20% was achieved, with the maximum up to 78.76% (Figure 3f). Eventually, the best device afforded a state-of-the-art PCE of 14.04% with a V_{OC} of 0.941 V, a J_{SC} of 19.06 mA cm^{-2}, and an FF of 78.32%. According to the EQE spectra as displayed in Figure 3c, the superior J_{SC} of PBDB-TF:IDIC-C4Ph-based optimal OSC mainly originates from the high response exceeding 80% between 640 and 725 nm (maximum: 83.5%, 670 nm) which mainly belongs to the absorption of IDIC-C4Ph (Figure 1b). The high EQE response of PBDB-TF:IDIC-C4Ph-based OSC indicates that efficient photoelectron conversion occurs in the device and the photons absorbed by IDIC-C4Ph are efficiently converted into electrons during the process of photoelectric conversion. Additionally, the devices were also treated with 0.5% (v/v) 1,8-diiodooctane (DIO) and displayed a slightly decreased PCE of 13.54%.

As for the three key photovoltaic parameters of OSCs, V_{OC} and J_{SC} could be predicted to a certain extent for the

comparatively specific connections with basic properties of donor/acceptor materials (including the energy levels, light-harvesting ability, etc.). However, it is difficult to predict the FF because of its unambiguous correlations with material chemical structures. Generally, FF is closely related to the charge mobilities, miscibility of the donor and acceptor, morphologies and molecular orientations of BHJ, charge generation and collection, etc., which are relatively difficult to be estimated from the basic properties of materials.[42] Thus, the approaches to improve FF is highly meaningful for the advance of OSCs. For instance, device optimization, including additives, thermal annealing, solvent annealing, as well as efficient transport layers, was often applied to regulate the morphologies of BHJ and increase the FFs and PCEs of OSCs.[43–48] From the point of the molecular design of SMAs, the side chain optimization from bulky aryl chains to compact alkyl chains has been proven to be valid to improve FF, which was again verified by the studies of IDIC-PhC6 and IDIC in this work. Notably, we provide a new insight about the side chain optimization of SMAs which could further enhance the FF over 78% and greatly boost the PCEs.

To gain deeper insight into the charge transport behaviors of OSCs, the charge mobilities were measured using the space charge-limited current (SCLC) method. From Table 2 and Figure S5 (Supporting Information), we noted that extremely unbalanced charge transport exists in PBDB-T:IDIC-PhC6-based devices, with hole (μ_h)/electron (μ_e) mobilities estimated to be $2.31 \times 10^{-4}/0.02 \times 10^{-4}$ cm^2 V^{-1} s^{-1}. The inferior electron mobility should be mainly ascribed to the poor crystallinity of IDIC-PhC6, and the unbalanced μ_h and μ_e could lead to increased charge recombination inside device. By contrast,

**ADVANCED
SCIENCE NEWS**
www.advancedsciencenews.com

**ADVANCED
MATERIALS**
www.advmat.de

PBDB-T:IDIC-based OSCs generated not only increased μ_h/μ_e of $2.42 \times 10^{-4}/2.90 \times 10^{-4}$ cm^2 V^{-1} s^{-1} but also more balanced charge mobilities ($\mu_e/\mu_h = 1.20$), which can partly explain the improved J_{SC} and FF. Inspiringly, both the hole and electron mobilities of PBDBT-:IDIC-C4Ph-based device were further enhanced simultaneously. The μ_h/μ_e reached $4.70 \times 10^{-4}/4.89 \times 10^{-4}$ cm^2 V^{-1} s^{-1} with an outstanding μ_e/μ_h value of 1.04, thus resulting in the most competitive J_{SC} and FF as well as PCEs among the three OSCs. Additionally, PBDB-TF:IDIC-C4Ph-based OSCs with and without thermal annealing were also detected. High and balanced charge transport with μ_h/μ_e of $2.21 \times 10^{-4}/2.66 \times 10^{-4}$ cm^2 V^{-1} s^{-1} is noted from the as-cast PBDB-TF:IDIC-C4Ph device, agree well with its high FF above 76%. After annealing, the hole/electron mobilities were increased to $3.48 \times 10^{-4}/4.51 \times 10^{-4}$ cm^2 V^{-1} s^{-1}, contributing to the further raised J_{SC} relative to the as-cast devices. As a contrast, the annealed OSC of PBDB-TF:IDIC affords lower hole mobility of 0.47×10^{-4} cm^2 V^{-1} s^{-1} than its as-cast device, which is probably related to the remarkable change of morphologies.

To probe the charge generation and dissociation process of OSCs, plots of photocurrent (J_{ph}) versus effective voltage (V_{eff}) were measured and are displayed in Figure S6a (Supporting Information). The parameter definitions are described in the Supporting Information. The exciton dissociation probability [$P_{diss}(E, T)$], which is correlated with the electric field (E) and temperature (T), is determined from the ratio of J_{ph}/J_{sat}.[49,50] Figure S6b (Supporting Information) exhibits the plots of P_{diss} versus V_{eff} at the short-circuit conditions ($V_{eff} = V_{OC}$). Relatively low P_{diss} of 76% was calculated from the IDIC-PhC6-based device, suggesting only three quarters of the total photo-generated e–h pairs dissociated into free charges, which agrees with the inferior efficiencies of OSCs. As a contrast, higher P_{diss} values were recorded from IDIC- and IDIC-C4Ph-based devices. Especially, the optimal devices of IDIC-C4Ph exhibit excellent P_{diss} over 95% under the short-circuit conditions. The higher P_{diss} signifies that OSCs with IDIC-C4Ph instead of IDIC-PhC6 and IDIC generated higher exciton dissociation and charge extraction efficiencies, which is well consistent with the superior PCEs of the related devices. Additionally, the correlation of V_{OC} with the light intensity was measured to evaluate the degree of recombination in three SMA-based devices.[51] The semilogarithmic plot of V_{OC} as a function of the light intensity is shown in Figure S7 (Supporting Information) and the parameter definitions are described in the Supporting Information. As Figure S7 (Supporting Information) reveals, slopes of $1.38 kT/q$ and $1.21 kT/q$ (where k is the Boltzmann constant, T is the temperature, and q is the elementary charge) were calculated from IDIC-PhC6- and IDIC-based solar cells, suggesting considerable trap-assisted recombination involved inside devices. As a contrast, a decreased slope of $1.13 kT/q$ was observed from OSC of IDIC-C4Ph, indicating a suppressed recombination of free carriers under the open-circuit condition.

Molecular stacking orientations in BHJ were further investigated by GIWAXS. As shown in **Figure 4**a–c, there optimized blend films reveal distinct stacking feature. Similar with the GIWAXS pattern of film IDIC-PhC6, weak edge-on stacking mode was found in PBDB-T:IDIC-PhC6 blend, consistent with the measured low electron mobility. Interestingly, despite that IDIC possesses stronger face-on stacking orientations than IDIC-C4Ph (Figure 2), only cognizable π–π stacking along the OOP direction was detected from PBDB-T:IDIC. In sharp contrast, well-defined diffraction plots with enhanced π–π stacking (010) as well as raised long-range orderly packing (100, 200, and 300) were observed from the OOP direction of PBDB-T:IDIC-C4Ph (Figure 4c,d). The multilevel better-organized molecular stacking especially the improved face-on orientation is considered to be a contributing factor for the improved J_{SC} and FF of PBDB-T:IDIC-C4Ph-fabricated OSCs. The improved molecular packing also supports the increase of charge transport as discussed above. Thus, we can conclude that the rationally weakened crystallization property of IDIC-C4Ph, contrarily, promoted the better molecular orderly stacking when blend with donor material.

To further explore the influence of SMA's crystallization property on BHJ morphologies, PBDB-T:IDIC-PhC6, PBDB-T:IDIC, and PBDB-T:IDIC-C4Ph at the optimized conditions were investigated by transmission electron microscopy (TEM) and atomic force microscopy (AFM). From the TEM images (Figure 4f–h) and AFM images (Figure S8, Supporting Information), three blends reveal distinctively different aggregation feature. Large domain clusters were found from PBDB-T:IDIC-PhC6 which could produce greatly increased charge recombination, leading to the inferior J_{SC} and FF. As for PBDB-T:IDIC blend (Figure 4g; Figure S8b, Supporting Information), rough morphology with a root-mean-square (RMS) roughness of 9.15 nm was observed accompanying with many regular aggregates which should be ascribed to the strong crystallization of IDIC during the spin-coating and thermal annealing process. The excessive aggregates inside BHJ could serve as charge traps and increase the charge recombination. As discussed above, IDIC-C4Ph exhibits moderately decreased crystallinity than IDIC. Meanwhile, the blend PBDB-T:IDIC-C4Ph demonstrates superior orderly molecular stacking and stronger face-on orientation than the PBDB-T:IDIC blend. As expected, well-distributed nanofiber interpenetrating networks with decreased RMS of 3.16 nm take shape in the PBDB-T:IDIC-C4Ph blend, while keeping some nanoscale aggregates with a diameter of about 20–50 nm (Figure 4h; Figure S8c, Supporting Information). We cannot confirm the role nanoscale aggregates played on the photovoltaic process, but this probably indicates that the crystallinity of IDIC-C4Ph could be further slightly reduced to give a more uniform blend. Nevertheless, considering the almost identical fabrication conditions (solvent, film thickness, thermal annealing temperature, time, etc.) of three blend films, we can draw the conclusion that the crystallization characteristic of SMAs have a remarkable influence on the BHJ morphologies, and the moderately weakened crystallization of the SMA could promote the BHJ to generate better morphologies.

Considering the different optimal conditions of PBDB-TF:IDIC-C4Ph and PBDB-TF:IDIC devices, we further make a detailed investigation about the molecular orientations and morphologies of these two blend films under as-cast and thermal annealing. The GIWAXS patterns are shown in **Figure 5**. The AFM and TEM images are displayed in **Figure 6** and Figure S9 (Supporting Information). As Figure 5a,c indicates, two as-cast blends show similar stacking mode with weak 010 diffraction plots in OOP direction. However, diverse morphology characteristics were found in these two as-cast blends. As
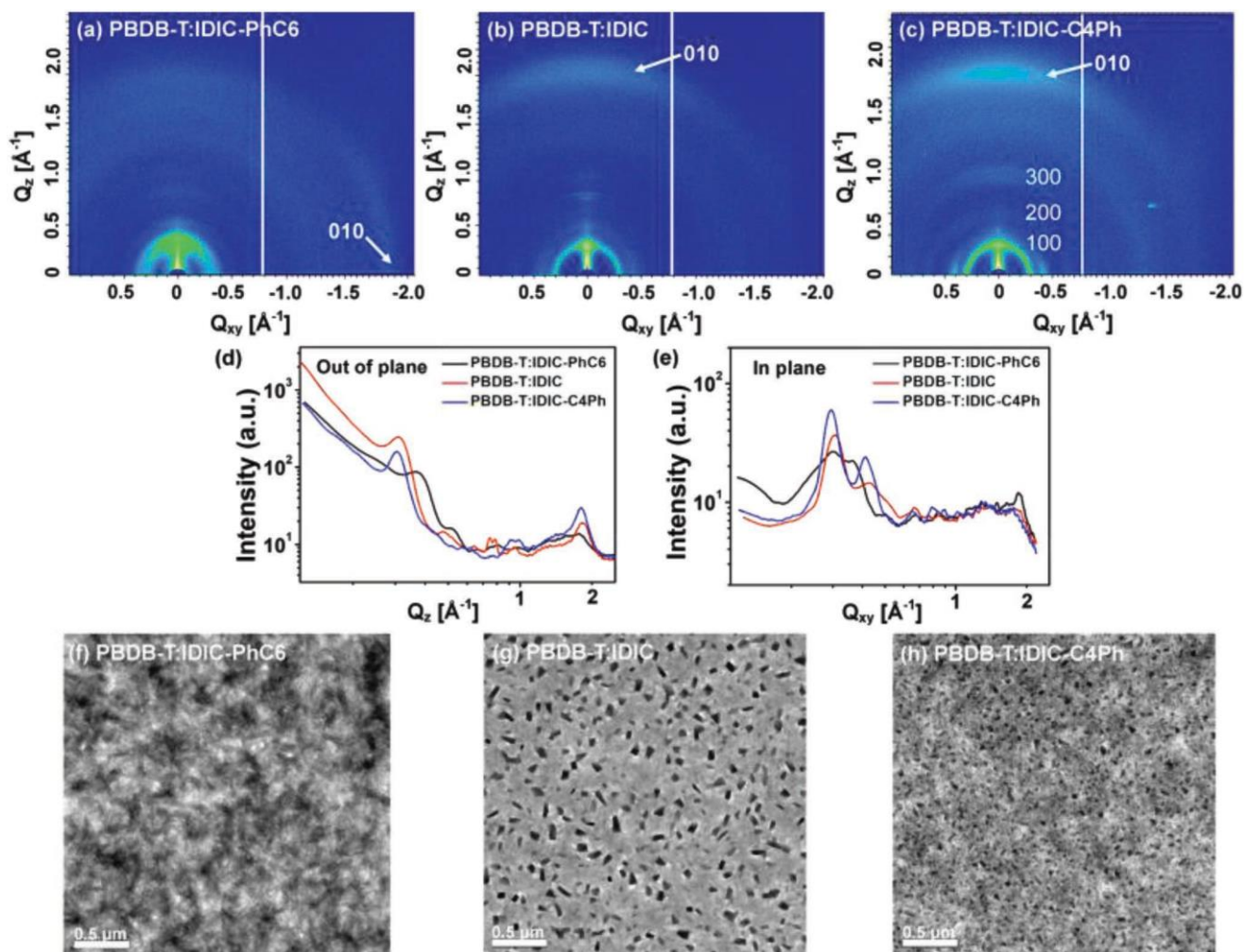
Figure 4. a–c) GIWAXS scattering patterns of blends PBDB-T:IDIC-PhC6, PBDB-T:IDIC, and PBDB-T:IDIC-C4Ph, and d,e) the line profiles. f–h) The respective TEM images.

shown in Figure 6a,e, numerous well-defined nanofibers were detected from PBDB-TF:IDIC-C4Ph as-cast film, indicating the preferred miscibility of the donor and acceptor. As reported, the fibril assembly can dictate the morphology framework which is highly advantageous in BHJ OSCs.[52] This partly contributes to the impressive FF approaching 77% as well as the PCE of 13.23% for PBDB-TF:IDIC-C4Ph-based as-cast OSCs. However, unfavorable cloudlike large clusters were observed from PBDB-TF:IDIC as-cast film (Figure 6c,g), probably ascribed to the instinct aggregation feature of IDIC. Thus, although the similar stacking orientations of two as-cast films, the ideal phase-separation behavior of PBDB-TF:IDIC-C4Ph could ensure the more efficient charge transport and separation in OSCs.

After PBDB-TF:IDIC-C4Ph being thermal annealed for 30 s, some nanoscale aggregates were assembled while still maintaining the nanofiber interpenetrating network with slightly increased RMS from 2.08 to 2.24 nm (Figure 6b,f). This was similar with the morphology of PBDB-T:IDIC-C4Ph annealed film (Figure 4h). Simultaneously, greatly improved face-on orientation and long-range orderly packing were observed from the OOP direction of PBDB-TF:IDIC-C4Ph (Figure 5b,e). This

synergistic variation of morphology and stacking mode after annealing witness enhanced hole/electron mobilities, improved J_{SC} and FF of OSCs with the optimal PCE of 14.04%. In sharp contrast, after PBDB-TF:IDIC was annealed for 30 s, the misty domains grow into rugged and irregular aggregates, accompanying with the RMS grown from 1.53 to 10.7 nm (Figure 6d,h). This significant change of BHJ morphology should be attributed to the strong aggregation tendency of IDIC especially after thermal annealing. Meanwhile, no obvious improvement of the molecular stacking was detected from the GIWAXS study (Figure 5d,e). The serious phase separation of annealed PBDB-TF:IDIC film undoubtedly negatively affected the charge transport and photovoltaic properties of OSCs. Thus the crystallization feature of SMAs not only play an important role in the BHJ morphology modulation of as-cast films but also afford different variation with the employment of thermal annealing.

To make an intuitive illustration about the adjust of side chains of SMAs on crystallization and BHJ properties, a schematic diagram was shown in **Figure 7**. IDIC-PhC6 reveals poor crystallinity duo to the serious steric hindrance of the bulky phenyl attached onto the main backbone. Amorphous
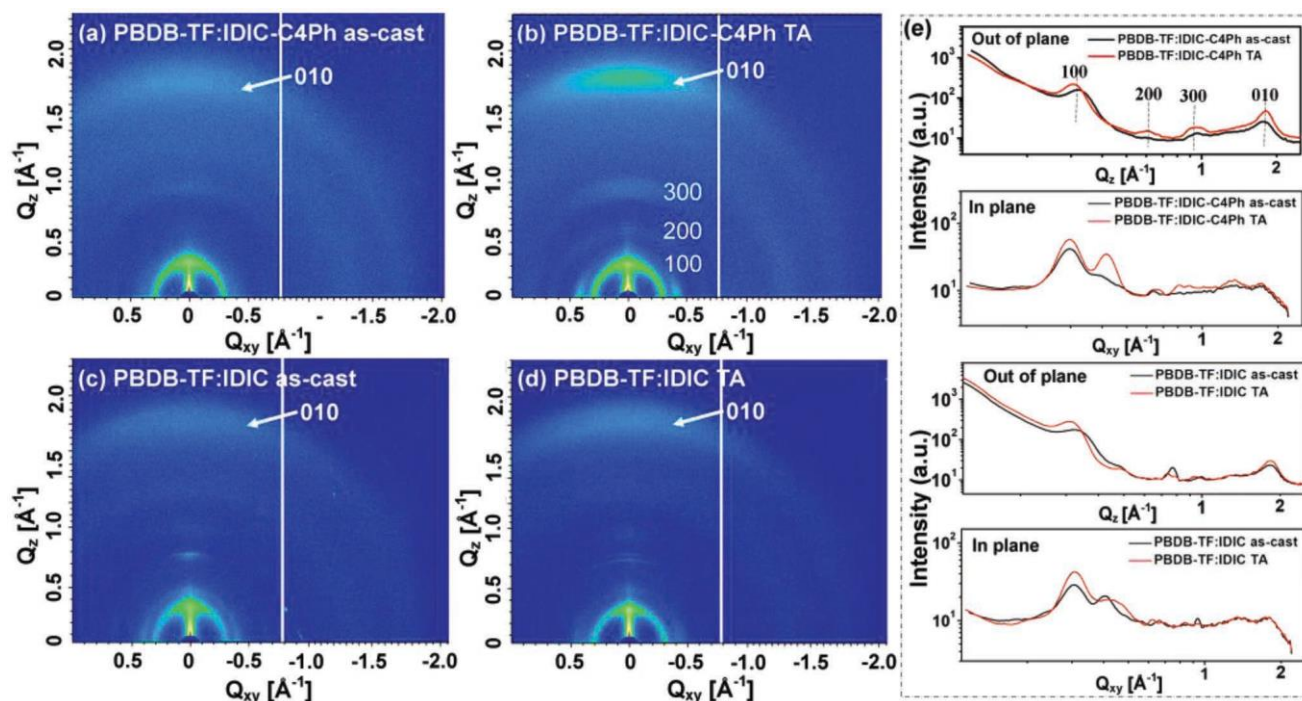
Figure 5. a–d) GIWAXS scattering patterns of blends PBDB-TF:IDIC-C4Ph and PBDB-TF:IDIC under different processing conditions and e) the respective line profiles.

stacking feature was observed in IDIC-PhC6 film as well as the BHJ blend, which in turn decreased the charge transport and afforded low photovoltaic properties. On the contrary, high crystallinity was found from IDIC originating from the ordered, compact alkyl side chains. As expected, strong face-on molecular orientation was detected from IDIC film, which ordinarily should be preferred by the OSC. However, this overly strong aggregation of IDIC leads to large domains in the as-cast blend, and serious phase separation with increased roughness and regular aggregates take shape after thermal annealing.
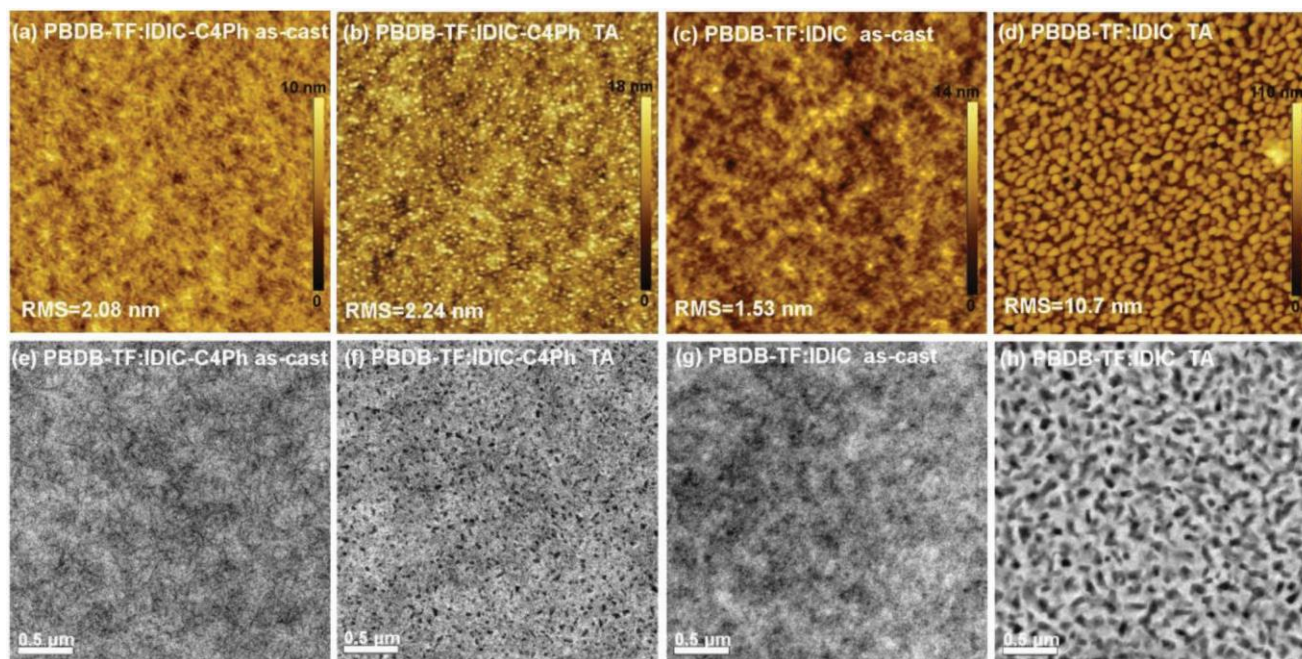
Figure 6. a–d) AFM topography images (5 μm × 5 μm) and e–h) TEM images of PBDB-TF:IDIC-C4Ph and PBDB-TF:IDIC blend films under different conditions.
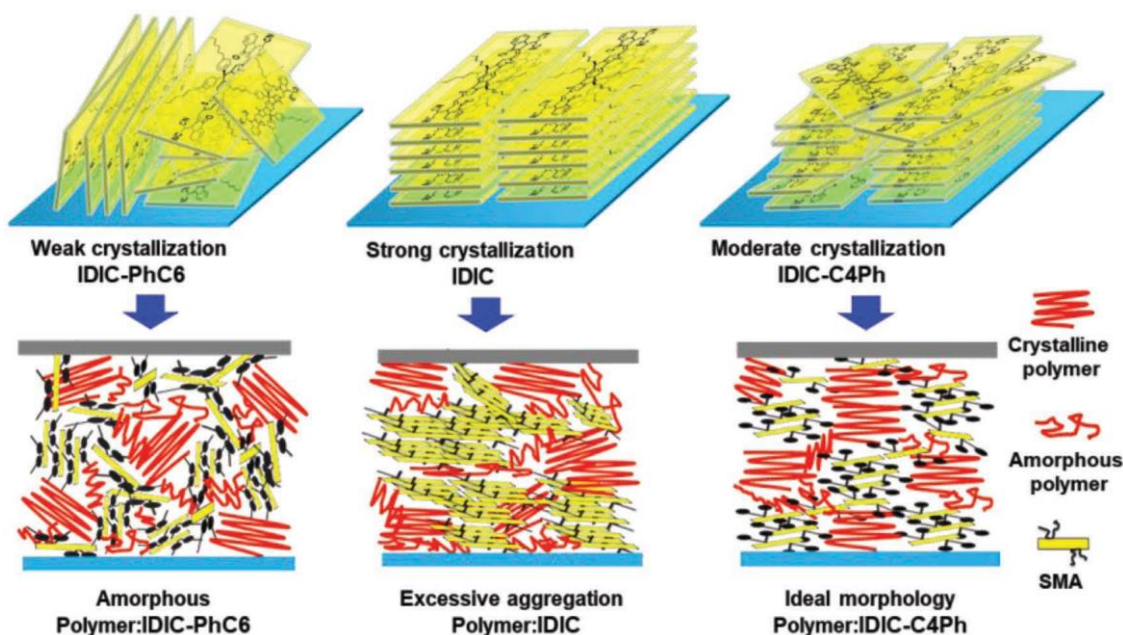
Figure 7. The schematic diagram of molecular stacking in pure SMA films and BHJ blends.

With a phenyl substitution at the tail of the alkyl side chain, IDIC-C4Ph generated moderate crystallization tendency owing to the synergistic regulation of the ordered alkyl side chain and the bulky phenyl terminal of the alkyl chain. As a consequence, modest weakened crystallization feature was verified relative to IDIC, while still keeping some fraction face-on orientation in IDIC-C4Ph pure film. Interestingly, despite the decreased crystallinity of IDIC-C4Ph, preferred stronger face-on orientations were detected from IDIC-C4Ph-based blend film. More importantly, well-distributed nanofiber interpenetrating networks were observed from both the as-cast and annealed blend film based on IDIC-C4Ph.

In summary, we have reported an effective approach via simple side chain modification to rationally modulate the property of SMAs to balance the crystallinity of acceptors and miscibility of bulk heterojunction. Specifically, a bulky phenyl (Ph)

was attached onto the tail of alkyl side chain (枯C_4H_9) which was linked to the backbone of SMA. The alkyl side chain was expected to keep the compact molecular stacking while the bulky phenyl terminal was expected to produce a disturbance to the molecular stacking through steric hindrance. As a result, moderate crystallization was found for IDIC-C4Ph, keeping the nearly uniform absorption feature and energy levels with IDIC. The rational decreased crystallization characteristics of IDIC-C4Ph afforded better morphologies and enhanced face-on orientation in BHJ blends. The PBDB-T:IDIC-C4Ph-based optimal device produced an impressive FF of 77.42% and high PCE of 11.50%, greater than the best OSCs based on IDIC-PhC6 (6.14%) and IDIC (10.41%). With PBDB-TF as the donor, outstanding efficiency of 13.23% was recorded from IDIC-C4Ph-based as-cast OSCs, with a high FF of 76.83%, the highest value among as-cast OSCs. After thermal annealing, the J_{SC} and FF of OSCs were further slightly improved. The champion device afforded a state-of-the-art PCE of 14.04% with a V_{OC} of 0.941 V, a J_{SC} of 19.06 mA cm^{-2}, and an outstanding FF of 78.32%. Particularly, different from the numerous reports focused on the enhancement of the crystallization of SMAs, this work provides an original insight for the crystallization modulation of SMAs. That is, the rational decreased crystallinity of SMA is fairly important to make a balance between material crystallinity and BHJ morphology. Honestly, there is no guarantee that 枯C_4H_9 alkyl side chain with the phenyl terminal of IDIC-C4Ph is the optimal combination for IDT-based SMAs. However, it indeed provides a valid method for crystallization and morphology regulation of SMAs. As shown in **Scheme 2**, the length of alkyl chains, types
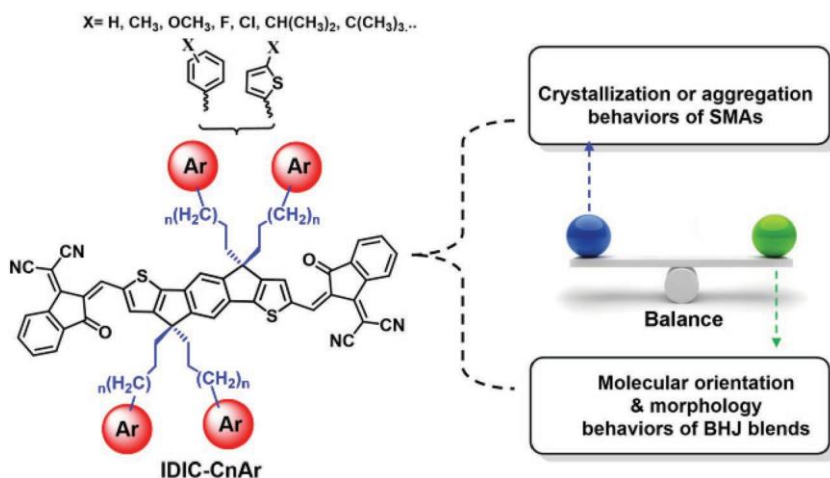
Scheme 2. The chemical structures of IDIC-CnAr-type SMAs.

of the terminal aryl groups, and the partnership of the alkyl chain and aryl terminal could probably further generate fascinating modulation effect on the SMA's basic properties as well as the photovoltaic performance of OSCs. Thus, we foresee further efficiency improvement through the rational design of the side chain of SMAs and the match of donor materials.

Supporting Information

Supporting Information is available from the Wiley Online Library or from the author.

Acknowledgements

Conflict of Interest

The authors declare no conflict of interest.

Keywords

[1] Y. Lin, J. Wang, Z. G. Zhang, H. Bai, Y. Li, D. Zhu, X. Zhan, *Adv. Mater.* **2015**, *27*, 1170.

[2] S. Li, L. Ye, W. Zhao, H. Yan, B. Yang, D. Liu, W. Li, H. Ade, J. Hou, *J. Am. Chem. Soc.* **2018**, *140*, 7159.

[3] T. Liu, Z. Luo, Q. Fan, G. Zhang, L. Zhang, W. Gao, X. Guo, W. Ma, M. Zhang, C. Yang, Y. Li, H. Yan, *Energy Environ. Sci.* **2018**, *11*, 3275.

[4] H. Zhang, H. Yao, J. Hou, J. Zhu, J. Zhang, W. Li, R. Yu, B. Gao, S. Zhang, J. Hou, *Adv. Mater.* **2018**, *30*, 1800613.

[5] Y. Lin, Q. He, F. Zhao, L. Huo, J. Mai, X. Lu, C.-J. Su, T. Li, J. Wang, J. Zhu, Y. Sun, C. Wang, X. Zhan, *J. Am. Chem. Soc.* **2016**, *138*, 2973.

[6] H. Feng, N. Qiu, X. Wang, Y. Wang, B. Kan, X. Wan, M. Zhang, A. Xia, C. Li, F. Liu, H. Zhang, Y. Chen, *Chem. Mater.* **2017**, *29*, 7908.

[7] Y. Ma, M. Zhang, Y. Yan, J. Xin, T. Wang, W. Ma, C. Tang, Q. Zheng, *Chem. Mater.* **2017**, *29*, 7942.

[8] S. Holliday, R. S. Ashraf, A. Wadsworth, D. Baran, S. A. Yousaf, C. B. Nielsen, C. H. Tan, S. D. Dimitrov, Z. Shang, N. Gasparini, M. Alamoudi, F. Laquai, C. J. Brabec, A. Salleo, J. R. Durrant, I. McCulloch, *Nat. Commun.* **2016**, *7*, 11585.

[9] B. Kan, J. Zhang, F. Liu, X. Wan, C. Li, X. Ke, Y. Wang, H. Feng, Y. Zhang, G. Long, R. H. Friend, A. A. Bakulin, Y. Chen, *Adv. Mater.* **2017**, *29*, 1704904.

[10] J. Zhu, Z. Ke, Q. Zhang, J. Wang, S. Dai, Y. Wu, Y. Xu, Y. Lin, W. Ma, W. You, X. Zhan, *Adv. Mater.* **2017**, *29*, 1704713.

[11] S. Dai, F. Zhao, Q. Zhang, T. K. Lau, T. Li, K. Liu, Q. Ling, C. Wang, X. Lu, W. You, X. Zhan, *J. Am. Chem. Soc.* **2017**, *139*, 1336.

[12] Z. Yao, X. Liao, K. Gao, F. Lin, X. Xu, X. Shi, L. Zuo, F. Liu, Y. Chen, A. K. Jen, *J. Am. Chem. Soc.* **2018**, *140*, 2054.

[13] B. Jia, S. Dai, Z. Ke, C. Yan, W. Ma, X. Zhan, *Chem. Mater.* **2018**, *30*, 239.

[14] S. Li, L. Ye, W. Zhao, S. Zhang, S. Mukherjee, H. Ade, J. Hou, *Adv. Mater.* **2016**, *28*, 9423.

[15] S. Li, L. Ye, W. Zhao, S. Zhang, H. Ade, J. Hou, *Adv. Energy Mater.* **2017**, *7*, 1700183.

[16] D. Xie, T. Liu, W. Gao, C. Zhong, L. Huo, Z. Luo, K. Wu, W. Xiong, F. Liu, Y. Sun, C. Yang, *Sol. RRL* **2017**, *1*, 1700044.

[17] Z. Luo, H. Bin, T. Liu, Z. G. Zhang, Y. Yang, C. Zhong, B. Qiu, G. Li, W. Gao, D. Xie, K. Wu, Y. Sun, F. Liu, Y. Li, C. Yang, *Adv. Mater.* **2018**, *30*, 1706124.

[18] W. Gao, M. Zhang, T. Liu, R. Ming, Q. An, K. Wu, D. Xie, Z. Luo, C. Zhong, F. Liu, F. Zhang, H. Yan, C. Yang, *Adv. Mater.* **2018**, *30*, 1800052.

[19] H. Yao, Y. Cui, R. Yu, B. Gao, H. Zhang, J. Hou, *Angew. Chem., Int. Ed.* **2017**, *56*, 3045.

[20] S. Yu, Y. Chen, L. Yang, P. Ye, J. Wu, J. Yu, S. Zhang, Y. Gao, H. Huang, *J. Mater. Chem. A* **2017**, *5*, 21674.

[21] W. Wang, B. Zhao, Z. Cong, Y. Xie, H. Wu, Q. Liang, S. Liu, F. Liu, C. Gao, H. Wu, Y. Cao, *ACS Energy Lett.* **2018**, *3*, 1499.

[22] R. Yu, S. Zhang, H. Yao, B. Guo, S. Li, H. Zhang, M. Zhang, J. Hou, *Adv. Mater.* **2017**, *29*, 1700437.

[23] S. J. Xu, Z. Zhou, W. Liu, Z. Zhang, F. Liu, H. Yan, X. Zhu, *Adv. Mater.* **2017**, *29*, 1704510.

[24] Y. Lin, F. Zhao, S. K. K. Prasad, J. D. Chen, W. Cai, Q. Zhang, K. Chen, Y. Wu, W. Ma, F. Gao, J. X. Tang, C. Wang, W. You, J. M. Hodgkiss, X. Zhan, *Adv. Mater.* **2018**, *30*, 1706363.

[25] Y. Yang, Z. G. Zhang, H. Bin, S. Chen, L. Gao, L. Xue, C. Yang, Y. Li, *J. Am. Chem. Soc.* **2016**, *138*, 15011.

[26] T. J. Aldrich, S. M. Swick, F. S. Melkonyan, T. J. Marks, *Chem. Mater.* **2017**, *29*, 10294.

[27] Y. Lin, F. Zhao, Q. He, L. Huo, Y. Wu, T. C. Parker, W. Ma, Y. Sun, C. Wang, D. Zhu, A. J. Heeger, S. R. Marder, X. Zhan, *J. Am. Chem. Soc.* **2016**, *138*, 4955.

[28] Z. Luo, C. Sun, S. Chen, Z.-G. Zhang, K. Wu, B. Qiu, C. Yang, Y. Li, C. Yang, *Adv. Energy Mater.* **2018**, *8*, 1800856.

[29] Z. Fei, F. D. Eisner, X. Jiao, M. Azzouzi, J. A. Rohr, Y. Han, M. Shahid, A. S. R. Chesman, C. D. Easton, C. R. McNeill, T. D. Anthopoulos, J. Nelson, M. Heeney, *Adv. Mater.* **2018**, *30*, 1705209.

[30] S. Feng, C. Zhang, Y. Liu, Z. Bi, Z. Zhang, X. Xu, W. Ma, Z. Bo, *Adv. Mater.* **2017**, *29*, 1703527.

[31] I. Meager, R. S. Ashraf, S. Mollinger, B. C. Schroeder, H. Bronstein, D. Beatrup, M. S. Vezie, T. Kirchartz, A. Salleo, J. Nelson, I. McCulloch, *J. Am. Chem. Soc.* **2013**, *135*, 11537.

[32] C. Cabanetos, A. El Labban, J. A. Bartelt, J. D. Douglas, W. R. Mateker, J. M. Frechet, M. D. McGehee, P. M. Beaujuge, *J. Am. Chem. Soc.* **2013**, *135*, 4656.

[33] J. Yao, C. Yu, Z. Liu, H. Luo, Y. Yang, G. Zhang, D. Zhang, *J. Am. Chem. Soc.* **2016**, *138*, 173.

[34] E. Al-Naamani, A. Gopal, M. Ide, I. Osaka, A. Saeki, *ACS Appl. Mater. Interfaces* **2017**, *9*, 37702.

[35] S.-H. Kang, H. R. Lee, G. K. Dutta, J. Lee, J. H. Oh, C. Yang, *Macromolecules* **2017**, *50*, 884.

[36] S. Vegiraju, B. C. Chang, P. Priyanka, D. Y. Huang, K. Y. Wu, L. H. Li, W. C. Chang, Y. Y. Lai, S. H. Hong, B. C. Yu, C. L. Wang, W. J. Chang, C. L. Liu, M. C. Chen, A. Facchetti, *Adv. Mater.* **2017**, *29*, 1702414.

[37] Z. Li, K. Jiang, G. Yang, J. Y. Lai, T. Ma, J. Zhao, W. Ma, H. Yan, *Nat. Commun.* **2016**, *7*, 13094.

**ADVANCED
SCIENCE NEWS**

www.advancedsciencenews.com

**ADVANCED
MATERIALS**

www.advmat.de

[38] H. Huang, L. Yang, A. Facchetti, T. J. Marks, *Chem. Rev.* **2017**, *117*, 10291.

[39] X. Li, T. Yan, H. Bin, G. Han, L. Xue, F. Liu, Y. Yi, Z.-G. Zhang, T. P. Russell, Y. Li, *J. Mater. Chem. A* **2017**, *5*, 22588.

[40] B. Gao, H. Yao, B. Jang, J. Zhu, R. Yu, Y. Cui, F. Wang, J. Hou, H. Y. Woo, J. Hou, *J. Mater. Chem. A* **2018**, *6*, 2664.

[41] Q. Fan, Y. Wang, M. Zhang, B. Wu, X. Guo, Y. Jiang, W. Li, B. Guo, C. Ye, W. Su, J. Fang, X. Ou, F. Liu, Z. Wei, T. C. Sum, T. P. Russell, Y. Li, *Adv. Mater.* **2018**, *30*, 1704546.

[42] X. Guo, N. Zhou, S. J. Lou, J. Smith, D. B. Tice, J. W. Hennek, R. P. Ortiz, J. T. L. Navarrete, S. Li, J. Strzalka, L. X. Chen, R. P. H. Chang, A. Facchetti, T. J. Marks, *Nat. Photonics* **2013**, *7*, 825.

[43] Y. Li, D. Liu, J. Wang, Z.-G. Zhang, Y. Li, Y. Liu, T. Zhu, X. Bao, M. Sun, R. Yang, *Chem. Mater.* **2017**, *29*, 8249.

[44] J. K. Lee, W. L. Ma, C. J. Brabec, J. Yuen, J. S. Moon, J. Y. Kim, K. Lee, G. C. Bazan, A. J. Heeger, *J. Am. Chem. Soc.* **2008**, *130*, 3619.

[45] W. Ma, C. Yang, X. Gong, K. Lee, A. J. Heeger, *Adv. Funct. Mater.* **2005**, *15*, 1617.

[46] X. Liu, W. Wen, G. C. Bazan, *Adv. Mater.* **2012**, *24*, 4505.

[47] J. J. van Franeker, M. Turbiez, W. Li, M. M. Wienk, R. A. Janssen, *Nat. Commun.* **2015**, *6*, 6229.

[48] Z. Zheng, Q. Hu, S. Zhang, D. Zhang, J. Wang, S. Xie, R. Wang, Y. Qin, W. Li, L. Hong, N. Liang, F. Liu, Y. Zhang, Z. Wei, Z. Tang, T. P. Russell, J. Hou, H. Zhou, *Adv. Mater.* **2018**, *30*, 1801801.

[49] J.-L. Wu, F.-C. Chen, Y.-S. Hsiao, F.-C. Chien, P. Chen, C.-H. Kuo, M. H. Huang, C.-S. Hsu, *ACS Nano* **2011**, *5*, 959.

[50] V. Shrotriya, Y. Yao, G. Li, Y. Yang, *Appl. Phys. Lett.* **2006**, *89*, 063505.

[51] B. Yang, S. Zhang, Y. Chen, Y. Cui, D. Liu, H. Yao, J. Zhang, Z. Wei, J. Hou, *Macromolecules* **2017**, *50*, 1453.

[52] T. Liu, L. Huo, S. Chandrabose, K. Chen, G. Han, F. Qi, X. Meng, D. Xie, W. Ma, Y. Yi, J. M. Hodgkiss, F. Liu, J. Wang, C. Yang, Y. Sun, *Adv. Mater.* **2018**, *30*, 1707353.